Mon. Not. R. Astron. Soc. **000**, 1–9 (2014) Printed 14 April 2016 (MN LATEX style file v2.2)

Identifying IGR J14091–6108 as a magnetic CV with a massive white dwarf using X-ray and optical observations

John A. Tomsick[1⋆], Farid Rahoui[2,3], Roman Krivonos[4], Maïca Clavel[1], Jay Strader[5], and Laura Chomiuk[5]

[1]*Space Sciences Laboratory, 7 Gauss Way, University of California, Berkeley, CA 94720-7450, USA*
[2]*European Southern Observatory, Karl Schwarzschild-Strasse 2, 85748 Garching bei Munchen, Germany*
[3]*Department of Astronomy, Harvard University, 60 Garden Street, Cambridge, MA 02138, USA*
[4]*Space Research Institute, Russian Academy of Sciences, Profsoyuznaya 84/32, 117997 Moscow, Russia*
[5]*Department of Physics and Astronomy, Michigan State University, East Lansing, MI 48824, USA*

14 April 2016

ABSTRACT

IGR J14091–6108 is a Galactic X-ray source known to have an iron emission line, a hard X-ray spectrum, and an optical counterpart. Here, we report on X-ray observations of the source with *XMM-Newton* and *NuSTAR* as well as optical spectroscopy with ESO/VLT and NOAO/SOAR. In the X-rays, this provides data with much better statistical quality than the previous observations, and this is the first report of the optical spectrum. Timing analysis of the *XMM* data shows a very significant detection of 576.3 ± 0.6 s period. The signal has a pulsed fraction of 30 ± 3% in the 0.3–12 keV range and shows a strong drop with energy. The optical spectra show strong emission lines with significant variability in the lines and continuum, indicating that they come from an irradiated accretion disk. Based on these measurements, we identify the source as a magnetic Cataclysmic Variable of Intermediate Polar (IP) type where the white dwarf spin period is 576.3 s. The X-ray spectrum is consistent with the continuum emission mechanism being due to thermal Bremsstrahlung, but partial covering absorption and reflection are also required. In addition, we use the IP mass (IPM) model, which suggests that the white dwarf in this system has a high mass, possibly approaching the Chandrasekhar limit.

Key words: stars: individual(IGR J14091–6108), white dwarfs, X-rays: stars, accretion, stars: novae, catalysmic variables

1 INTRODUCTION

The hard X-ray imaging by the *International Gamma-Ray Astrophysics Laboratory (INTEGRAL)* satellite (Winkler et al. 2003) has led to the discovery of a large number of new or previously poorly studied "IGR" sources. The most recent published catalogs of 17–100 keV sources detected by *INTEGRAL* include more than 900 sources for the whole sky (Bird et al. 2016) and ∼400 sources within 17.5° of the Galactic plane (Krivonos et al. 2012). A large fraction of the sources have been identified as Active Galactic Nuclei (AGN), Cataclysmic Variables (CVs), High-Mass X-ray Binaries (HMXBs), Low-Mass X-ray Binaries (LMXBs), and Pulsar Wind Nebulae (PWNe), but 23% of the 939 sources listed in Bird et al. (2016) are still unidentified, in part due to the difficulty in finding counterparts at other wavelengths with the ∼1′–4′ *INTEGRAL* position uncertainties. In an effort to characterize the populations of hard X-ray sources in the Galaxy, we have been performing follow-up observations of sources in the Galactic Plane to identify the natures of as many IGR sources as possible.

During 2013–2015, we observed ten IGR sources with the *Chandra X-ray Observatory*, and the results were reported in Tomsick et al. (2015) and Tomsick et al. (2016). In some cases, the information from the *Chandra* observation, including accurate source positions that provided optical or IR identifications, immediately led to a determination of the nature of the source. For example, IGR J04059+5416 and IGR J08297–4250 were identified as AGN (Tomsick et al. 2015), and IGR J18088–2741 was identified as a CV (Tomsick et al. 2016). IGR J14091–6108 was one of the sources observed in this program, but the *Chandra* observation did not allow us to definitively determine its nature, and we selected it for further study as described in this work.

IGR J14091–6108 was discovered when it was detected in the *INTEGRAL* 9-year Galactic Hard X-ray Survey (Krivonos et al. 2012). A *Swift* X-ray counterpart was found by Landi et al. (2012) and then the source was observed with *Chandra*, leading to the detection of a strong iron Kα emission line in the X-ray spectrum and

⋆ E-mail: jtomsick@ssl.berkeley.edu (JAT)

the identification of an optical/IR counterpart (Tomsick et al. 2014, 2016). *Chandra* showed that the source has a hard power-law continuum with a photon index of $\Gamma = 0.6 \pm 0.4$, suggesting an accreting compact object with a high magnetic field strength (Tomsick et al. 2016). While we favored a magnetic CV, we did not rule out the possibility that the source is an HMXB. In this work, we use new X-ray and optical observations to study IGR J14091–6108 in more detail.

2 OBSERVATIONS AND DATA REDUCTION

Table 1 lists the observations that we used, including simultaneous X-ray observations with the *X-ray Multi-Mirror Mission (XMM-Newton)* and the *Nuclear Spectroscopic Telescope Array (NuSTAR)* as well as optical spectroscopy with the Very Large Telescope (VLT[1]) and with the Southern Astrophysical Research Telescope (SOAR). The X-ray observations occurred on 2015 July 20-21, and the observation identifiers (ObsIDs), exact start and stop times, and exposure times are provided in Table 1. The X-ray data provide a large improvement in the statistical quality over the previous *Chandra* and *INTEGRAL* observations to give better constraints on the spectrum and to allow for a sensitive search for periodic signals. The optical data provide a first look at the spectrum of the source. In the following, we describe how the data from each facility were reduced.

2.1 *XMM*

For the EPIC/pn (Strüder et al. 2001) and EPIC/MOS (Turner et al. 2001) instruments, we reduced the data using the *XMM* Science Analysis Software v14.0.0 to make images, light curves, and spectra. For pn, we made a full-field 10–12 keV light curve to look for times of high background, and filtered these times out for the final data products. We followed the same procedure for MOS and obtained slightly more time on-source (28.9 ks for MOS compared to 24.7 ks for pn). In addition to the time filtering, we used the standard event filtering described in procedures that are available online[2]. We extracted source counts from a circular region with a radius of 40″ centered on IGR J14091-6108 and estimated the background using a rectangular region on parts of the detectors with no sources. After background subtraction, the 0.3–12 keV count rates for pn, MOS1, and MOS2 are 0.207 ± 0.003, 0.059 ± 0.015, and 0.065 ± 0.016 c/s, respectively. We included 1% systematic errors on the pn and MOS source spectra when fitting the energy spectra to account for calibration uncertainties. We examined the data from the Reflection Grating Spectrometer (RGS), but the count rate for this instrument is too low to be useful.

2.2 *NuSTAR*

For *NuSTAR* (Harrison et al. 2013), we reduced the data using HEASOFT v6.17, which includes NUSTARDAS v1.5.1. The calibration files are from the 2015 March 16 version of the calibration database (CALDB). We ran `nupipeline` to produce event lists for the two *NuSTAR* instruments: focal plane modules A and B (FPMA and FPMB). We examined the full band images, and extracted light curves and spectra with `nuproducts` using a circular source region with a radius of 60″. Although the *NuSTAR* images do not show any significant stray light, spatial variations in the background are visible, which is expected. Thus, we estimated the background using `nuskybgd` (Wik et al. 2014), which is a package of IDL programs that sample the background over the field of view outside of the source region to model the spatial variations. We produced the model and then used it to estimate the background in the source region. We included 4% systematic errors on the background spectrum. After background subtraction, the 3–79 keV source count rates are 0.076 ± 0.002 and 0.075 ± 0.002 c/s for FPMA and FPMB, respectively. Finally, when producing the final spectra for fitting, we grouped the energy bins to give a significance of greater than 5-σ.

2.3 Optical Spectroscopy

We obtained low-resolution spectroscopy of the IGR J14091–6108 counterpart identified in Tomsick et al. (2016), which is CXOU J140846.0–610754 and VVV J140845.99–610754.1. We used the FORS2 instrument with the 300V and 300I grisms combined with the GC435 and OG590 filters, respectively. In both cases, the slit-width was set to 1″, giving a $R \sim 600$ average resolution. Atmospheric conditions were medium-to-good, with a thin sky, seeing at 500 nm in the range 0.″6-0.″8, and an airmass between 1.1 and 1.3. The integration time of each individual frame was set to 600 s and 500 s for the 300V, and 300I grisms, respectively, and two exposures were taken in each grism. The A0V spectro-photometric standard star CD-32 9927 was observed in similar conditions for flux-calibration. We reduced the data using the dedicated pipeline (v. 5.1.4) implemented in the ESO data reduction environment `Reflex` v. 2.6, following the standard steps for optical spectroscopy reduction to produce a cleaned, flatfielded, wavelength- and flux-calibrated 1D spectrum.

We also obtained several optical spectra on UT 2015 January 15 using the Goodman High-Throughput Spectrograph (Clemens et al. 2004) on the SOAR 4.1-m telescope. All data were taken with a 1.03″ slit. We obtained one 600 sec exposure using the 400 l mm^{-1} grating (wavelength coverage ∼3000–7000 Å; resolution 5.7 Å) and two 600 sec exposures using the 1200 l mm^{-1} grating (wavelength coverage 5480–6740 Å; resolution 1.7 Å). These data were wavelength calibrated with an FeAr arc lamp and were bias corrected using the overscan region. The spectra were optimally extracted using routines in IRAF.

3 RESULTS

3.1 X-ray Timing

We produced 0.3–12 keV event lists for the three *XMM* instruments, including only the photons in a 40″ circular region centered on the position of IGR J14091–6108. The times of the individual events were shifted to the solar system barycenter using the SAS tool `barycen`. We used the Z_1^2 (Rayleigh) test (Buccheri et al. 1983) to make periodograms from the event list. We searched for a periodic signal in the pn data by making a periodogram with 20000 time bins between 1 and 2000 s. One significant peak is present with a peak value of $S = 134$ (see Figure 1a). The false alarm probability (FAP) is given by $0.5\, e^{-S/2}$ multiplied by the number of trials, corresponding to a FAP of 8.5×10^{-26}. The period is 576.3 ± 0.6 s, where the 1-σ errors are given by the periods where the periodogram has

[1] We carried out the observations under ESO program identifier 095.D-0972(A).

[2] see http://xmm.esac.esa.int/sas/current/documentation/threads/

fallen to $S-1$. The MOS1 and MOS2 instruments showed significant peaks at 575.9 ± 0.8 s and 577.1 ± 1.3 s, respectively, which are both consistent with the period measured by pn (Figure 1a). We produced a folded light curve, which is shown in Figure 1b. An epoch of zero phase (minimum in the folded light curve) is MJD TDB 57224.0971 ± 0.0003. To align the *XMM* and *NuSTAR* phases, we barycentered the *NuSTAR* event lists and folded the *NuSTAR* photons on the *XMM* ephemeris.

We calculated the pulsed fraction of the signal by defining maximum and minimum phase ranges using the 0.3–12 keV folded light curve (Figure 1b). The pulsed fraction is defined as the absolute value of the difference between the maximum and minimum count rate divided by the sum of these quantities. In the 0.3–12 keV range, it is $30 \pm 3\%$. The folded light curves from 0.3 to 79 keV are shown in Figure 2, and the values for the pulsed fraction are indicated on Figure 2 and plotted in Figure 3. The *XMM* measurements show a strong decrease in the pulsed fraction with energy with the largest drop being at 7 keV. The *NuSTAR* measurements also show a drop with energy, with a pulsed fraction of $13 \pm 4\%$ in the 3–12 keV band and $0 \pm 6\%$ (no detection) in the 12–79 keV band.

A period of 576 s is fairly typical for the spin period of a white dwarf in a CV of Intermediate Polar (IP) type. In the 2014 update of the Ritter & Kolb (2003) CV catalog[3], there are 78 IP-type CVs (CV/IPs) with white dwarf spin periods between 128 and 12071 s, and 20 systems have periods faster than 576 s. The shortest CV/IP orbital period is 1552 s, and the median orbital period is 4.1 hr. Thus, if IGR J14091–6108 is a CV/IP, the detected period is much more likely to be the white dwarf spin period, and the orbital period is probably between several and ∼100 times longer (Hong et al. 2012)

3.2 Optical Spectra

Figure 4 displays the flux-calibrated SOAR/Goodman (magenta) and VLT/FORS2 (blue) spectra of IGR J14091−6108, on which all the detected spectroscopic features are marked. Likewise, Table 2 lists their main parameters, i.e. their central wavelengths (λ_c), equivalent widths ($\mathring{W}$), full-widths at half-maximum (FWHM), and intrinsic fluxes ($F_{\rm Line}$), obtained through single-Gaussian fitting. The FWHMs were quadratically corrected for the instrumental broadening and the underlying continua were locally assessed with a first-order polynomial. The continuum level being the primary source of inaccuracy, each measurement was repeated several times with different placements within the same wavelength range to obtain a set of values that eventually averaged out. The listed uncertainties are therefore the scatter to the mean rather than just statistical.

The optical spectrum is very rich, with a wealth of spectral features that includes the Balmer and Paschen series as well as several signatures of He I and He II, all in emission. The Bowen Blend at 4640 Å, typical of irradiated accretion disks and/or companion stars in accreting systems, is also clearly observed with FORS2 and perhaps with Goodman. The spectrum also appears to be strongly variable, the continuum and emission lines being roughly fives and three times brighter in the Goodman spectrum, respectively.

Besides features intrinsic to IGR J14091−6108, we also report two diffuse interstellar bands (DIBs) centered at 5780 Å and 6284 Å. DIBs are strongly correlated to the ISM extinction along the line-of-sight of the sources in which they are detected and we can assess the latter using the relationships between their equivalent widths and $E(B-V)$ given in Jenniskens & Desert (1994). Nonetheless, DIB6284 is likely contaminated with some atmospheric absorption troughs and we therefore rely on DIB5780 only, for which Jenniskens & Desert (1994) obtain $\frac{\mathring{W}}{E(B-V)} = 0.647 \pm 0.053$. We measure $\mathring{W}_{5780} = 0.97 \pm 0.11$ and $\mathring{W}_{5780} = 1.11 \pm 0.07$ in the Goodman and FORS2 spectra, respectively, which, once averaged out, leads to $E(B-V) = 1.615 \pm 0.166$. Using the relationship $A_V = R_V \times E(B-V)$ and an average total-to-selective extinction ratio $R_V = 3.1$, we thus derive $A_V = 5.01 \pm 0.51$, which is roughly consistent with a distance between 3 and 4 kpc based on the 3D Galactic extinction map derived in Marshall et al. (2006) for a line-of-sight 9.″4 away from that of IGR J14091−6108.

With the knowledge of A_V, it is now possible to correct IGR J14091−6108 emission from the ISM extinction and Figure 5 displays the extinction-corrected Goodman and FORS2 spectra expressed in Hz vs mJy. The first result is that both continua are roughly best-fit with power laws with 2.29 and 2.09 spectral indices, respectively, typical of the Raleigh-Jeans tail of a black body emitter. We can also estimate the Balmer decrements and we find Hα/Hβ = 1.03 ± 0.20 from the FORS2 spectrum as well as Hα/Hβ = 1.20 ± 0.23, Hγ/Hβ = 1.07 ± 0.26, Hδ/Hβ = 1.03 ± 0.27, Hϵ/Hβ = 0.86±0.27, and Hη/Hβ = 1.38±0.32 from the Goodman spectrum. It is clear that all the values are consistent with unity, which is typical of Cataclysmic Variables (CVs) and some microquasars (see, e.g., Williams 1980; Williams & Shipman 1988; Rahoui et al. 2014). Based on the wealth of emission lines, spectral variability, Raleigh-Jeans continuum, and flat Balmer decrements around unity, it is thus very likely that the optical emission of IGR J14091−6108 originates in an optically-thick irradiated accretion disk in a CV.

3.3 X-ray Spectrum

For spectral analysis, we jointly fitted the *XMM* (pn, MOS1, and MOS2) and *NuSTAR* (FPMA and FPMB) data in the 0.3–79 keV energy range. We used the XSPEC package (Arnaud 1996) and performed the fitting with χ^2 minimization. We fitted with an absorbed power-law model, using Wilms et al. (2000) abundances and Verner et al. (1996) cross sections for the absorption. We also allowed for normalization differences between instruments by introducing a multiplicative constant. Thus, the overall model in XSPEC notation was `constant*tbabs*pegpwrlw`. This showed that the spectrum is hard with $\Gamma \sim 0.8$, but the fit was poor with $\chi^2 = 1242$ for 346 degrees of freedom (dof). The largest residuals appear in the iron line region, indicating a strong emission line. Adding a Gaussian with $E_{\rm line} = 6.56 \pm 0.04$ keV and $\sigma_{\rm line} = 0.35 \pm 0.05$ keV provides a large improvement in the fit (to $\chi^2/\nu = 711/343$), but negative residuals in the high energy part of the spectrum indicate curvature in the spectrum and possibly a cutoff.

We changed the continuum model from a power-law to a thermal Bremsstrahlung component to allow for curvature in the model and also because this is the emission mechanism that is thought to operate in CV/IPs. While the model `constant*tbabs*(gaussian+bremss)` does not provide a good fit to the data ($\chi^2/\nu = 997/343$), partial covering absorption is typically used when fitting CV/IPs (Suleimanov et al. 2005; Mukai et al. 2015), and, in our case, using `pcfabs` with $N_{\rm H} = (1.4 \pm 0.3) \times 10^{23}$ cm^{-2} and a covering fraction of $0.68^{+0.02}_{-0.03}$ improves the fit greatly to $\chi^2/\nu = 516/341$. With this model, the Bremsstrahlung temperature is very high, $kT > 167$ keV (90% con-

[3] see http://vizier.u-strasbg.fr/viz-bin/VizieR-3?-source=B/cb/cbdata

fidence limit), but there are still residuals at the high energy end that we suspect are related to the presence of a reflection component.

Reflection of the hard X-ray emission off the white dwarf surface is often included in models when fitting CV/IP spectra, and recent work with *XMM* and *NuSTAR* spectra show strong evidence for this component in three other CV/IPs (Mukai et al. 2015). For IGR J14091–6108, we added a reflection component using the `reflect` model in XSPEC. This model is based on Magdziarz & Zdziarski (1995), which is for reflection of direct emission from neutral material and includes the dependence on viewing angle. By convolving `bremss` with `reflect`, the model includes both a direct and a reflected Bremsstrahlung component where the strength of the reflected component depends on the amplitude parameter, $\Omega/2\pi$. In our case, if the reflection amplitude is left as a free parameter, it will increase to values above 1.0. However, assuming that we see 100% of the direct emission, values of $\Omega/2\pi$ above unity are not physically possible for reflection from the white dwarf surface. Thus, we fix the reflection amplitude to 1.0, resulting in a fit with $\chi^2/\nu = 472/339$. The spectrum fit with this model is shown in Figure 6, and the parameters are given in Table 3. Although the Bremsstrahlung temperature drops when the reflection component is added, we still measure $kT = 81^{+31}_{-20}$ keV, which, as we discuss in Section 4, is high for a CV/IP. For this fit, the 0.3–79 keV unabsorbed (i.e., with the interstellar but not the partial covering column density set to zero) flux is 1.1×10^{-11} erg cm^{-2} s^{-1}.

While the actual reflection component has three main features: the Compton hump above 10 keV, the iron edge at 7.1 keV (for neutral iron), and an iron fluorescence line at 6.4 keV (also for neutral iron), the Magdziarz & Zdziarski (1995) model only includes the first two features, which is one reason that we include the Gaussian in the model above. If the emission line was due only to reflection from the white dwarf surface, we would expect a relatively narrow line centered at 6.4 keV; however, as shown in Table 3, we measure a broad line with $\sigma_{\rm line} = 0.28 \pm 0.04$ keV at an energy above 6.4 keV ($E_{\rm line} = 6.59 \pm 0.04$ keV). It is very likely that this is due to contributions from higher ionization states coming from the hot material in the accretion column, and this is common for CV/IPs (Hellier & Mukai 2004). We modified the model to include two lines with energies fixed to 6.4 keV (neutral iron) and 6.7 keV (He-like iron). This more physical representation of the emission lines provides an equivalently good fit ($\chi^2/\nu = 473/339$), but the lines are still relatively broad ($\sigma_{\rm line} = 0.24 \pm 0.05$ keV). Adding a third line at 6.97 keV (H-like iron) improves the fit ($\chi^2/\nu = 458/338$), and these lines are significantly narrower ($\sigma_{\rm line} = 0.07 \pm 0.04$ keV), which is consistent with line widths measured for other CV/IPs (Hellier & Mukai 2004). The line normalizations in Table 3 include 90% confidence uncertainties, suggesting that all the lines are significantly detected. Thus, the three-line model is very likely the correct interpretation based on the match between measured and expected line widths as well as on statistical grounds. In this model, the equivalent widths of the three lines are 320 ± 60, 160 ± 40, and 170 ± 50 eV for neutral, He-like, and H-like iron, respectively.

To explore the possible physical cause of the high temperature derived from the fitting the continuum with a Bremsstrahlung model, we replaced the Bremsstrahlung component with the IP mass (IPM) model of Suleimanov et al. (2005). For the IPM model, the hardness and cutoff energy of the predicted spectrum are both set by the white dwarf mass, and the only two free parameters are $M_{\rm WD}$ and the normalization. Physically, this connection between the $M_{\rm WD}$ and the spectrum is related to the maximum shock temperature in the accretion column (Suleimanov et al. 2005; Hailey et al., submitted to ApJ). The emission mechanism is still Bremsstrahlung, but the model includes a range of temperatures. The results for a model including direct and reflected IPM components, partial covering, and three Gaussians are reported in Table 4. As before, we fix the reflection amplitude to 1.0, and the other reflection parameters are consistent to the values found in the Bremsstrahlung fits. Also, there is little or no change in the continuum absorption and the emission line parameters. The IPM model parameters imply a high white dwarf mass, $M_{\rm WD} > 1.38\,M_{\odot}$. The components of the spectrum are shown in Figure 7.

We note that none of the models we have used provide formally acceptable fits, with the best one having a reduced-χ^2 of 1.36 for 338 dof. Mukai et al. (2015) obtained similar fit qualities for his *XMM+NuSTAR* spectra of CV/IPs and suggested that it is related to calibration differences between instruments, and this is also a possibility in our case. However, we explored some possibilities for improving the fits. For example, the fit improves if we start with the model given in Table 4 and allow $\Omega/2\pi$ to increase above 1.0. Although likely unphysical, the fit improves from a reduced-χ^2 of 1.42 (for 338 dof) to 1.33 (for 337 dof) at $\Omega/2\pi = 5.0$. Also, allowing the reflection component to dominate at high energies causes the IPM component to soften, and, for the extreme assumption that $\Omega/2\pi = 5.0$, $M_{\rm WD}$ drops to $1.2\,M_{\odot}$. The fit can also be improved by modifying the modeling of the absorption. In some CV/IPs, there is evidence for complex absorption patterns, and other authors have modeled this with two partial coverers (e.g., Beardmore et al. 2000). Adding a second partial coverer to the 3 Gaussian Bremsstrahlung model in Table 3 improves the reduced-χ^2 from 1.36 (for 338 dof) to 1.23 (for 336 dof). Although this is a significant improvement, this model leads to an interstellar column density of $N_{\rm H} = (0.16 \pm 0.10) \times 10^{22}$ cm^{-2}, which is much lower than the value implied by our measured optical extinction. Using the relation from Güver & Özel (2009), an A_V of 5.0 ± 0.5 magnitudes corresponds to $N_{\rm H} = (1.1 \pm 0.1) \times 10^{22}$ cm^{-2}. Thus, while both high reflection amplitude and additional partial covering absorption lead to improved fits, the former is not consistent with the physical scenario and the latter leads to unrealistically low values for the interstellar column density.

To avoid the complexities of the low energy part of the spectrum, we also explored fitting just the *NuSTAR* spectrum above 10 keV. Fitting with a Bremsstrahlung model gives a reduced-χ^2 of 1.62 for 37 dof, and the 90% confidence lower limit on the temperature is 112 keV. Adding a reflection component with $\Omega/2\pi = 1$, which makes the model `constant*reflect*bremss`, provides a good fit (reduced-$\chi^2 = 1.14$ for 35 dof), and the Bremsstrahlung temperature is 66^{+33}_{-22} keV. With `constant*reflect*ipm` and $\Omega/2\pi = 1$, we find $M_{\rm WD} > 1.31\,M_{\odot}$, which is consistent with the high mass values we obtain when fitting the entire spectrum.

4 DISCUSSION

The results indicate that we can identify IGR J14091–6108 as a CV/IP with a high degree of confidence. The 576.3 ± 0.6 s periodicity shows that there is a magnetized compact object in the system, and the hardness of the X-ray spectrum is typical of only a CV/IP or an accreting pulsar in an HMXB. The optical spectrum is dominated by an optically-thick irradiated accretion disk, and no evidence for emission from the companion star is found, indicating that it must be a low-mass star and ruling out the HMXB possibility. There is also strong long-term optical variability in the continuum and emission lines, the origin of which is not clear. IPs are known to be strongly variable in the optical regime and often show

large spectroscopic modulations associated with the spin period of the white dwarf and/or the orbital period (see e.g. Still et al. 1998; Belle et al. 2003; Scaringi et al. 2011). While this may be the case for IGR J14091−6108, especially for the spectral lines, we believe that the large brightness difference between the FORS2 and Goodman optical spectra is mainly due to different accretion rates within the accretion disk.

The X-ray spectrum is also consistent with a CV/IP, and we confirm the presence of the strong iron line originally reported by Tomsick et al. (2016) using *Chandra* measurements. With *XMM*, we find that the line emission is consistent with being a combination of lines from three ionization states with widths of 0.07 ± 0.04 keV and equivalent widths in the 160–320 eV range. These values are typical of iron line complexes seen in CV/IPs (Hellier & Mukai 2004). Also, combining the 0.3–79 keV flux of 1.1×10^{-11} erg cm^{-2} s^{-1} with our estimated distance of 3–4 kpc from the optical extinction, we obtain an X-ray luminosity of $1.6 \times 10^{34}\, d^2_{3.5\,\mathrm{kpc}}$ erg s^{-1}, which is consistent with expectations for CV/IPs. In the Bird et al. (2016) catalog, there are 40 confirmed and seven candidate CV/IPs. Of the confirmed systems, 18 have IGR names, making IGR J14091–6108 the 19th confirmed CV/IP discovered by *INTEGRAL* (Bird et al. 2016). However, we note that IGR J14091–6108 itself is not in the Bird et al. (2016) catalog, suggesting the possible presence of a much larger number of CV/IPs close to the *INTEGRAL* detection limit.

The strong drop in the pulsed fraction with energy that we see for IGR J14091–6108 has been seen for other CV/IPs. Taylor et al. (1997) report this energy dependence for the CV/IPs AO Psc and V1223 Sgr. For V1223 Sgr, phase-resolved spectroscopy shows that the energy dependence is primarily related to changes in the column density of absorbing material local to the CV (Hayashi et al. 2011), and we suspect that this is also the case for IGR J14091–6108.

While IGR J14091–6108 is typical of CV/IPs in many respects, it is a candidate system for having a higher than typical white dwarf mass. Using the IP Mass model that Suleimanov et al. (2005) applied to 14 CV/IPs, we obtain a mass in excess of $1.3\,M_\odot$ for IGR J14091–6108, while Suleimanov et al. (2005) find masses between $0.50 \pm 0.05\,M_\odot$ (for EX Hya) and $1.00 \pm 0.20\,M_\odot$ (for V1062 Tau). Yuasa et al. (2010) also used spectral fitting to estimate white dwarf masses for 17 CV/IPs, and they found masses as high as $\sim$1.2 $M_\odot$ for V709 Cas, PQ Gem, and NY Lup. Hailey et al. (submitted) fit spectra from several X-ray satellites including *NuSTAR* for the CV/IP IGR J17303–0601, which has a relatively massive white dwarf. With the *NuSTAR* spectrum, partial covering absorption, and reflection, they measured a white dwarf mass of $1.16 \pm 0.12\,M_\odot$. If they replaced the IPM model with a Bremsstrahlung model, they obtained a temperature of 34 ± 2 keV. From this comparison, the temperature of 81^{+31}_{-20} keV (or 66^{+33}_{-22} keV for the >10 keV fit) that we measure for IGR J14091–6108 is suggestive of mass in excess of $\sim$1.2 $M_\odot$. Hailey et al. discuss the CV/IP spectra in the context of the diffuse hard X-ray emission from the Galactic center (Perez et al. 2015), which may be caused by an unresolved population of magnetic CVs with white dwarfs that are more massive than the average Galactic population (Krivonos et al. 2007).

One reason for interest in massive white dwarfs is the question of whether the progenitors of type Ia supernovae (SNe) are merging white dwarfs or accreting white dwarfs that detonate when they reach the Chandrasekhar limit. Based on the relatively low soft X-ray luminosities from nearby elliptical galaxies and galaxy bulges, Gilfanov & Bogdán (2010) and Di Stefano (2010a) argue that <5% of type Ia SNe are from accreting white dwarfs (although subsequent works showed that the X-rays could be attenuated by stellar winds, accretion winds, or white dwarf atmospheres; Di Stefano 2010b; Nielsen et al. 2013a). Along these same lines, pre-explosion imaging of individual nearby type Ia SNe place interesting constraints on accreting and nuclear-burning white dwarfs as the SN progenitors (Liu et al. 2012; Nielsen et al. 2012, 2013b, 2014; Graur et al. 2014). On the other hand, the white dwarfs in CVs are, on average, more massive than white dwarfs that have not undergone mass accretion from a companion (Zorotovic et al. 2011), implying that accretion leads to a significant increase in the masses of the white dwarfs. Given the possibility that IGR J14091–6108 may harbor a white dwarf with a mass very close to the Chandrasekhar limit, follow-up observations to measure M_{WD} using other techniques should be high priority. Based on the 576 s spin period, an orbital period of several hours would be expected, and optical photometry might be used to search for this period. It may then be possible to obtain a radial velocity curve, but this may need to be done in the near-IR where we might see absorption lines from the companion star's photosphere.

ACKNOWLEDGMENTS

We would like to thank D. Wik for help with using `nuskybgd` to produce a background spectrum for *NuSTAR*. We also thank C. Hailey, J. Hong, and F. Fornasini for useful discussions. FR thanks the ESO staff who performed the service observations. JAT acknowledges partial support from NASA under *XMM* Guest Observer grant NNX15AW09G. MC acknowledges partial support under NASA Contract NNG08FD60C for work on the *NuSTAR* mission. This work was partially supported by NASA *Fermi* grant NNX15AU83G. RK acknowledges support from Russian Science Foundation (grant 14-22-00271). This work made use of data from the *NuSTAR* mission, a project led by the California Institute of Technology, managed by the Jet Propulsion Laboratory, and funded by the National Aeronautics and Space Administration. We thank the *NuSTAR* Operations, Software and Calibration teams for support with the execution and analysis of these observations. This research has made use of the *NuSTAR* Data Analysis Software (NuSTARDAS) jointly developed by the ASI Science Data Center (ASDC, Italy) and the California Institute of Technology (USA). Based on observations obtained at the Southern Astrophysical Research (SOAR) telescope, which is a joint project of the Ministério da Ciência, Tecnologia, e Inovação (MCTI) da República Federativa do Brasil, the U.S. National Optical Astronomy Observatory (NOAO), the University of North Carolina at Chapel Hill (UNC), and Michigan State University (MSU).

REFERENCES

Arnaud K. A., 1996, in Astronomical Society of the Pacific Conference Series, Vol. 101, Astronomical Data Analysis Software and Systems V, Jacoby G. H., Barnes J., eds., p. 17

Beardmore A. P., Osborne J. P., Hellier C., 2000, MNRAS, 315, 307

Belle K. E., Howell S. B., Sion E. M., Long K. S., Szkody P., 2003, ApJ, 587, 373

Bird A. J. et al., 2016, arXiv:1601.06074

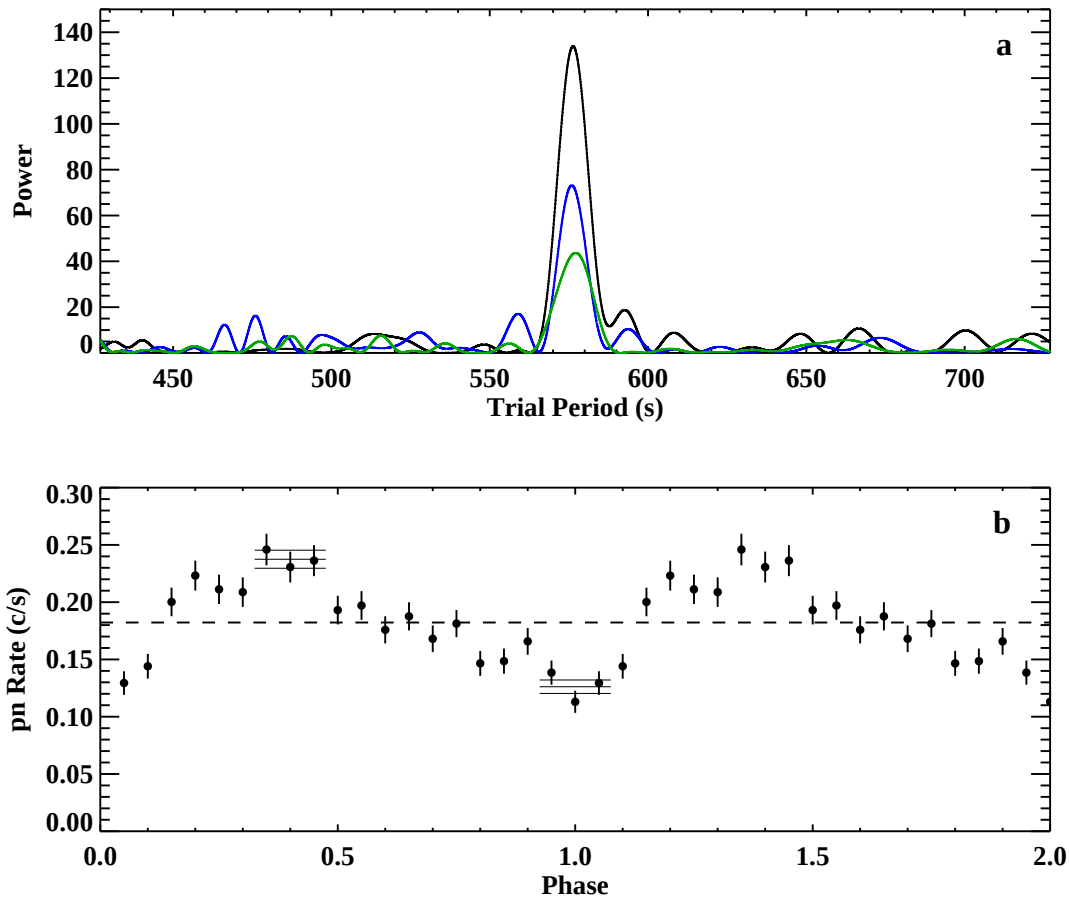

Figure 1. *(a)* Periodograms for 0.3–12 keV light curves from *XMM* pn (black), MOS1 (blue), and MOS2 (green), showing the detection of a signal at 576.3 ± 0.6 s. For the periodogram, the power is calculated using the Z_1^2 test. *(b)* Folded pn light curve in the 0.3–12 keV band. The horizontal solid lines indicate the phases used to determine the maximum and minimum rates. The difference between the maximum and minimum count rates divided by the sum of the maximum and minimum rates is the pulsed fraction.

Table 1. Observations of IGR J14091–6108

Observatory	ObsID	Instrument	Start Time (UT)	End Time (UT)	Exposure Time (ks)
XMM	0761940301	pn	2015 July 21, 2.22 h	2015 July 21, 10.03 h	24.7
”	”	MOS1	2015 July 21, 1.89 h	2015 July 21, 10.15 h	28.9
”	”	MOS2	”	”	”
NuSTAR	30101001002	FPMA	2015 July 20, 21.85 h	2015 July 21, 10.52 h	22.9
”	”	FPMB	”	”	”
VLT	095.D-0972(A)	FORS2	2015 April 13, 6.64 h	2015 April 13, 7.49 h	2.2
SOAR	—	Goodman Spectrograph	2015 January 15, 8.45 h	2015 January 15, 8.62 h	0.60

Buccheri R. et al., 1983, A&A, 128, 245
Clemens J. C., Crain J. A., Anderson R., 2004, in Society of Photo-Optical Instrumentation Engineers (SPIE) Conference Series, Vol. 5492, Ground-based Instrumentation for Astronomy, Moorwood A. F. M., Iye M., eds., pp. 331–340
Di Stefano R., 2010a, ApJ, 712, 728
Di Stefano R., 2010b, ApJ, 719, 474
Gilfanov M., Bogdán Á., 2010, Nature, 463, 924
Graur O., Maoz D., Shara M. M., 2014, MNRAS, 442, L28
Güver T., Özel F., 2009, MNRAS, 400, 2050
Harrison F. A. et al., 2013, ApJ, 770, 103
Hayashi T., Ishida M., Terada Y., Bamba A., Shionome T., 2011, PASJ, 63, S739
Hellier C., Mukai K., 2004, MNRAS, 352, 1037
Hong J., van den Berg M., Grindlay J. E., Servillat M., Zhao P., 2012, ApJ, 746, 165
Jenniskens P., Desert F.-X., 1994, A&AS, 106, 39
Kalberla P. M. W., Burton W. B., Hartmann D., Arnal E. M., Bajaja E., Morras R., Pöppel W. G. L., 2005, A&A, 440, 775
Krivonos R., Revnivtsev M., Churazov E., Sazonov S., Grebenev

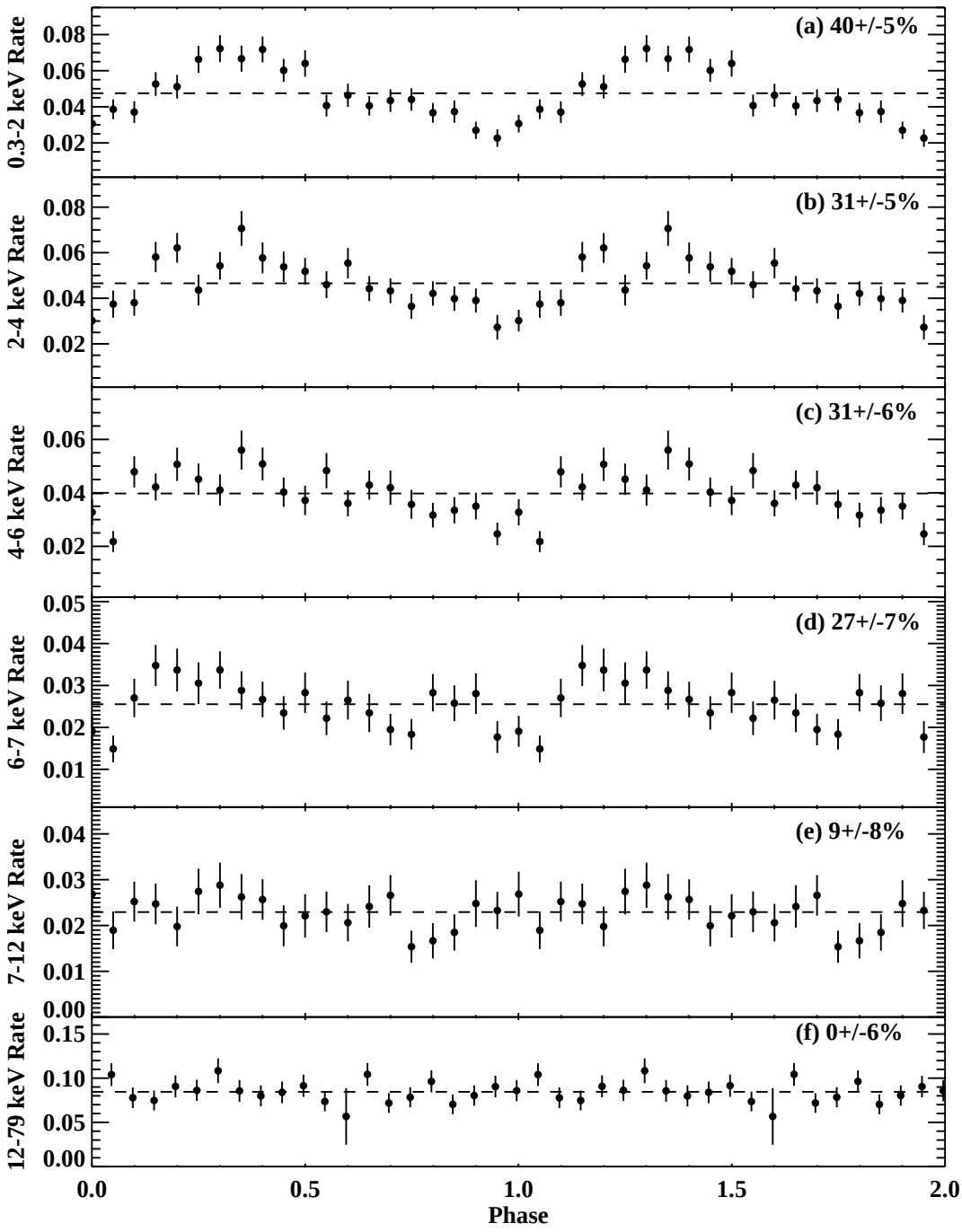

Figure 2. The X-ray light curves folded on the 576.3 s period. Panels *(a)-(e)* show folded light curves for five *XMM* pn energy bands, and panel *(f)* shows the 12–79 keV band from *NuSTAR*. Each panel shows the calculated value of the pulsed fraction with its 1-σ uncertainty. The same values are plotted vs. energy in Figure 3.

S., Sunyaev R., 2007, A&A, 463, 957

Krivonos R., Tsygankov S., Lutovinov A., Revnivtsev M., Churazov E., Sunyaev R., 2012, A&A, 545, A27

Landi R., Bassani L., Masetti N., Bazzano A., Fiocchi M., Bird A. J., Drave S., 2012, The Astronomer's Telegram, 4165, 1

Liu J., Di Stefano R., Wang T., Moe M., 2012, ApJ, 749, 141

Magdziarz P., Zdziarski A. A., 1995, MNRAS, 273, 837

Marshall D. J., Robin A. C., Reylé C., Schultheis M., Picaud S., 2006, A&A, 453, 635

Mukai K., Rana V., Bernardini F., de Martino D., 2015, ApJ, 807, L30

Nielsen M. T. B., Dominik C., Nelemans G., Voss R., 2013a, A&A, 549, A32

Nielsen M. T. B., Gilfanov M., Bogdán Á., Woods T. E., Nelemans G., 2014, MNRAS, 442, 3400

Nielsen M. T. B., Voss R., Nelemans G., 2012, MNRAS, 426,

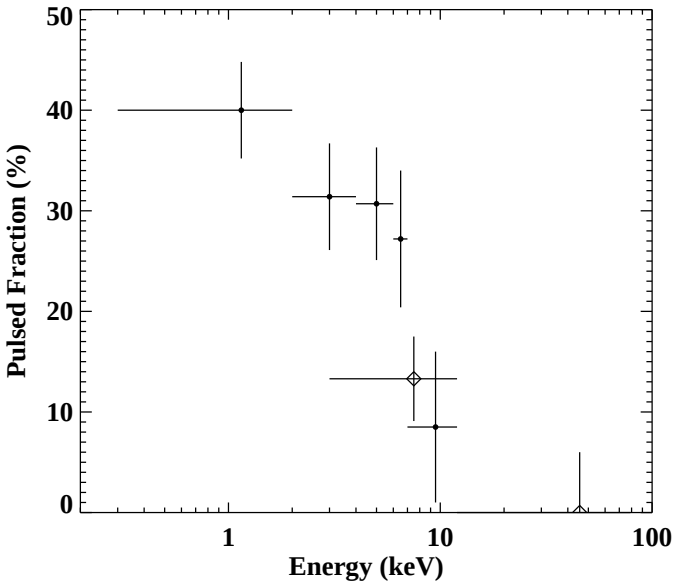

Figure 3. The pulsed fraction of the 576.3 s period versus energy. The filled circles mark the *XMM* pn measurements, and the diamonds mark the *NuSTAR* (FPMA+FPMB) measurements. The errors shown are 1-σ.

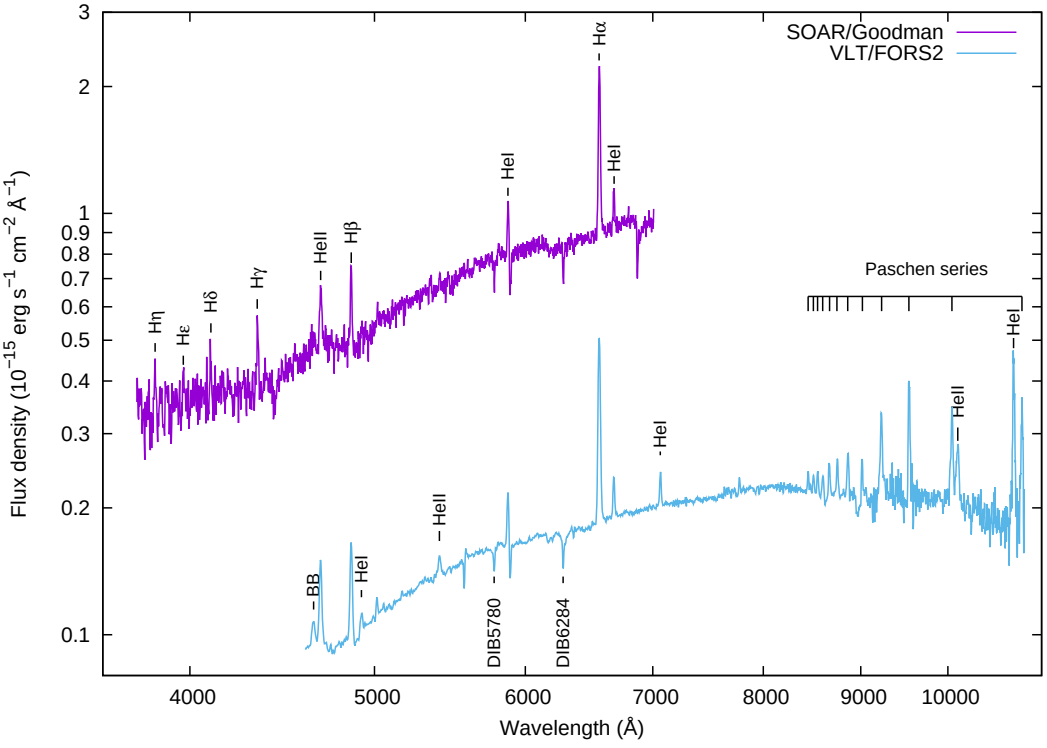

Figure 4. Two optical spectra of the IGR J14091–6108 counterpart (VVV J140845.99–610754.1). The purple spectrum was taken at SOAR in 2015 January with the Goodman spectrograph, and the light blue spectrum was taken in 2015 April at VLT with the FORS2 spectrograph. The emission lines from the source, and the lines due to interstellar absorption are labeled. See Table 2 for detailed line information and parameters.

2668
Nielsen M. T. B., Voss R., Nelemans G., 2013b, MNRAS, 435, 187
Perez K. et al., 2015, Nature, 520, 646
Rahoui F., Coriat M., Lee J. C., 2014, MNRAS, 442, 1610
Ritter H., Kolb U., 2003, A&A, 404, 301
Scaringi S. et al., 2011, A&A, 530, A6
Still M. D., Duck S. R., Marsh T. R., 1998, MNRAS, 299, 759
Strüder L. et al., 2001, A&A, 365, L18
Suleimanov V., Revnivtsev M., Ritter H., 2005, A&A, 435, 191

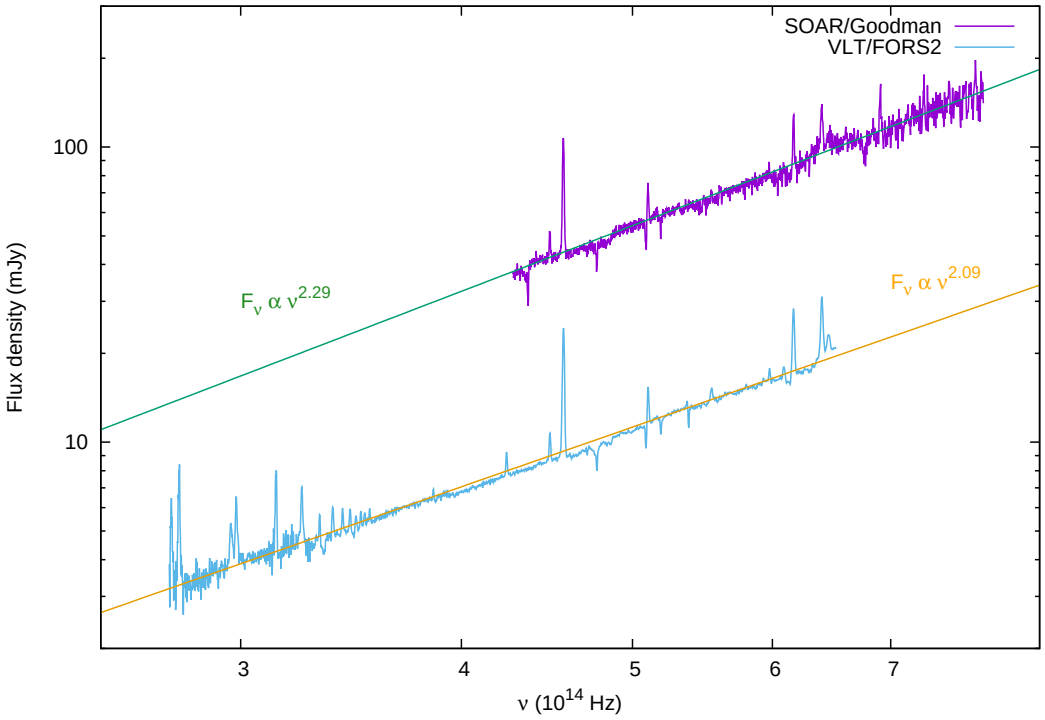

Figure 5. The same SOAR and VLT optical spectra of IGR J14091–6108 as shown in Figure 4. The spectra are dereddened, shown as a function of frequency, and the continua are each compared to a power-law function.

Taylor P., Beardmore A. P., Norton A. J., Osborne J. P., Watson M. G., 1997, MNRAS, 289, 349
Tomsick J. A., Krivonos R., Rahoui F., Ajello M., Rodriguez J., Barrière N., Bodaghee A., Chaty S., 2015, MNRAS, 449, 597
Tomsick J. A., Krivonos R., Wang Q., Bodaghee A., Chaty S., Rahoui F., Rodriguez J., Fornasini F. M., 2016, ApJ, 816, 38
Tomsick J. A., Rahoui F., Krivonos R., Rodriguez J., Bodaghee A., Chaty S., 2014, The Astronomer's Telegram, 6793, 1
Turner M. J. L. et al., 2001, A&A, 365, L27
Verner D. A., Ferland G. J., Korista K. T., Yakovlev D. G., 1996, ApJ, 465, 487
Wik D. R. et al., 2014, ApJ, 792, 48
Williams G. A., Shipman H. L., 1988, ApJ, 326, 738
Williams R. E., 1980, ApJ, 235, 939
Wilms J., Allen A., McCray R., 2000, ApJ, 542, 914
Winkler C. et al., 2003, A&A, 411, L1
Yuasa T., Nakazawa K., Makishima K., Saitou K., Ishida M., Ebisawa K., Mori H., Yamada S., 2010, A&A, 520, A25
Zorotovic M., Schreiber M. R., Gänsicke B. T., 2011, A&A, 536, A42

This paper has been typeset from a TEX/ LATEX file prepared by the author.

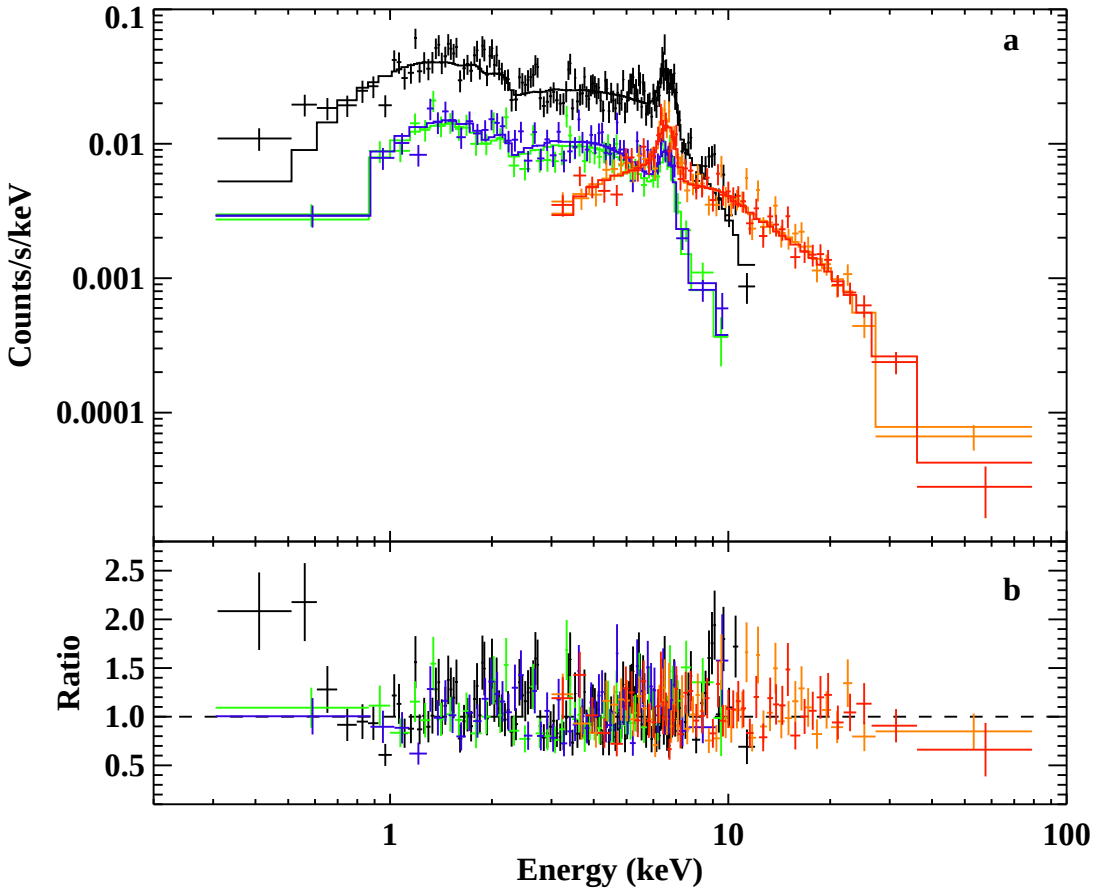

Figure 6. *(a) XMM* and *NuSTAR* energy spectrum (folded through the instrument response) fitted with a model consisting of `constant*tbabs*pcfabs*(gaussian+reflect*bremss)`. The black, light green, and blue spectra are for the *XMM* pn, MOS1, and MOS2 instruments, respectively. The orange and red spectra are for *NuSTAR* FPMA and FPMB, respectively. *(b)* The residuals in terms of the data-to-model ratio.

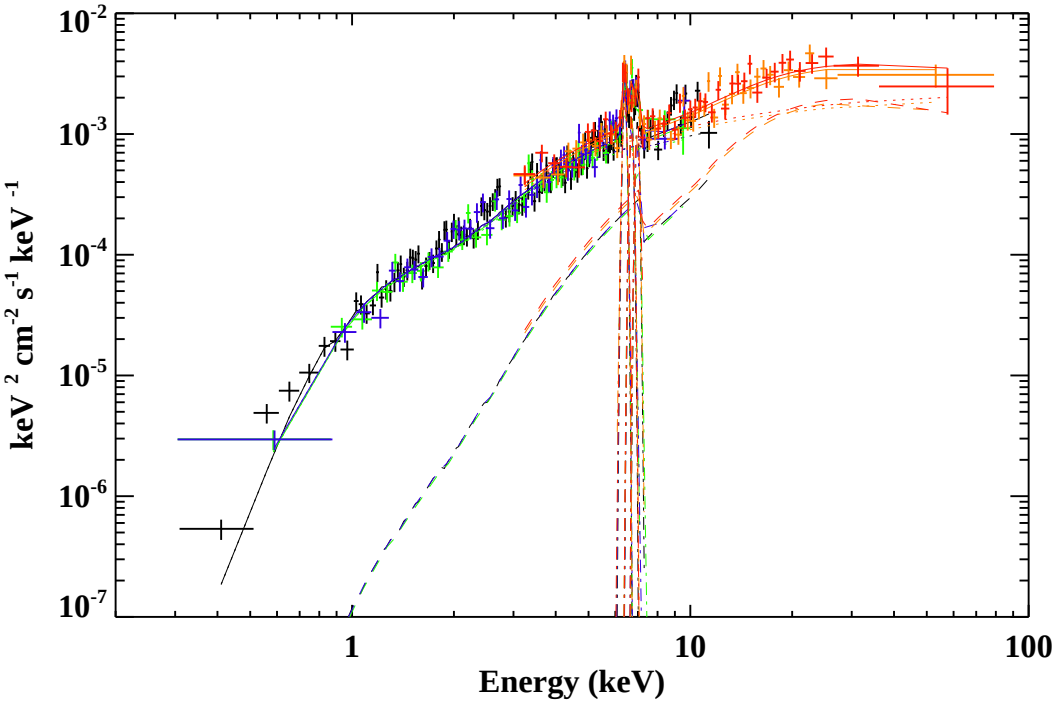

Figure 7. Unfolded *XMM* and *NuSTAR* energy spectrum fitted with the IP Mass model fit shown in Table 4. The components are 3 Gaussians *(dash-dotted lines)*, reflection *(dotted line)*, and the IP Mass model *(dashed)*. The spectra are plotted using the same colors as for Figure 6.

Table 2. Optical lines in the IGR J14091−6108 FORS2 and Goodman spectra.

		FORS2			Goodman		
Element	λ_c[a]	$\mathring{W}$[b]	FWHM[c]	F_{line}[d]	$\mathring{W}$	FWHM	F_{line}
Hη	3835	–	–	–	−3.4 ± 0.7	637 ± 96	1.10 ± 0.20
Hϵ	3968	–	–	–	−2.4 ± 1.0	579 ± 307	0.84 ± 0.25
Hδ	4101	–	–	–	−2.3 ± 0.6	281 ± 78	0.83 ± 0.20
Hγ	4341	–	–	–	−5.4 ± 1.2	690 ± 145	2.00 ± 0.37
BB[e]	4645	–3.2±1.1	1090±135	0.31±0.12	–	–	–
He II	4684	–9.7±2.8	666±72	0.93±0.23	−5.9 ± 0.9	856 ± 95	2.78 ± 0.38
Hβ	4861	–10.1±0.8	539±51	1.02±0.07	−5.4 ± 1.1	494 ± 43	2.94 ± 0.27
He I	4922	–1.1±0.3	523±48	0.12±0.04	–	–	–
He II	5409	-1.6±0.4	551±72	0.25±0.04	–	–	–
He I	5875	–4.9±0.9	353±57	0.83±0.05	−4.0 ± 0.5	492 ± 82	3.21 ± 0.44
Hα	6561	–37.6±1.5	652±45	6.84±0.12	−26.5 ± 1.8	707 ± 19	23.67 ± 1.90
He I	6678	–4.2±0.5	370±52	0.77±0.03	−3.3 ± 0.4	589 ± 53	3.30 ± 0.36
H I	7065	–3.4±0.3	354±43	0.67±0.04	–	–	–
H I	8446	–2.1±0.5	313±36	0.42±0.04	–	–	–
H I	8500	–1.5±0.1	362±19	0.34±0.03	–	–	–
H I	8543	–2.2±0.3	401±51	0.48±0.06	–	–	–
H I	8597	–2.0±0.4	377±40	0.46±0.06	–	–	–
H I	8663	–3.5±0.5	402±39	0.76±0.05	–	–	–
H I	8749	–3.7±0.5	437±30	0.82±0.03	–	–	–
H I	8862	–5.4±0.6	507±39	1.17±0.14	–	–	–
H I	9015	–3.8±0.7	420±51	0.83±0.34	–	–	–
H I	9228	–14.1±1.0	520±107	3.02±0.25	–	–	–
H I	9543	–19.0±3.9	515±36	4.23±0.29	–	–	–
H I	10050	–14.6±3.2	676±93	3.33±0.80	–	–	–
He II	10118	–9.7±3.2	881±123	2.23±0.78	–	–	–
H I	10828	–35.4±7.0	606±100	7.20±0.88	–	–	–
H I	10938	–21.8±6.2	652±113	4.39±0.68	–	–	–

[a] Measured wavelength in Å
[b] Equivalent widths in Å
[c] Full-width at half-maximum in km s^{-1}, quadratically corrected for instrumental broadening
[d] Intrinsic line flux in units of 10^{-15} erg cm^{-2} s^{-1}
[e] The Bowen Blend, which is the C III+N III complex.

Table 3. Spectral Results for Bremsstrahlung Fits

Parameter[a]	Units	1 Gaussian[b]	2 Gaussians[c]	3 Gaussians[d]
$N_{\rm H}$[e]	10^{22} cm^{-2}	$0.45^{+0.09}_{-0.08}$	”	”
$N_{\rm H,pc}$	10^{22} cm^{-2}	8^{+3}_{-2}	”	”
pc fraction	—	$0.65^{+0.04}_{-0.05}$	”	”
kT	keV	81^{+31}_{-20}	”	”
$N_{\rm bremss}$[f]	—	$(4.4^{+0.4}_{-0.3}) \times 10^{-4}$	”	”
$\Omega/2\pi$	—	1.0[g]	”	”
A[h]	—	$0.24^{+0.33}_{-0.16}$	”	”
$A_{\rm Fe}$[i]	—	1.0[g]	”	”
cos i	—	>0.70	”	”
$E_{\rm line1}$	keV	6.59 ± 0.04	6.4[g]	6.4[g]
$\sigma_{\rm line1}$	keV	0.28 ± 0.04	0.24 ± 0.05	0.07 ± 0.04
$N_{\rm line1}$	ph cm^{-2} s^{-1}	$(2.3 \pm 0.3) \times 10^{-5}$	$(0.86^{+0.27}_{-0.29}) \times 10^{-5}$	$(1.0 \pm 0.2) \times 10^{-5}$
$EW_{\rm line1}$	eV	940 ± 120	230 ± 80	320 ± 60
$E_{\rm line2}$	keV	—	6.7[g]	6.7[g]
$\sigma_{\rm line2}$	keV	—	0.24[j]	0.07[j]
$N_{\rm line2}$	ph cm^{-2} s^{-1}	—	$(1.4 \pm 0.3) \times 10^{-5}$	$(0.65 \pm 0.16) \times 10^{-5}$
$EW_{\rm line2}$	eV	—	470 ± 100	160 ± 40
$E_{\rm line3}$	keV	—	—	6.97[g]
$\sigma_{\rm line3}$	keV	—	—	0.07[j]
$N_{\rm line3}$	ph cm^{-2} s^{-1}	—	—	$(0.51 \pm 0.15) \times 10^{-5}$
$EW_{\rm line3}$	eV	—	—	170 ± 50
$C_{\rm pn}$	—	1.0[g]	”	”
$C_{\rm MOS1}$	—	0.96 ± 0.05	”	”
$C_{\rm MOS2}$	—	1.01 ± 0.05	”	”
$C_{\rm FPMA}$	—	1.11 ± 0.07	”	”
$C_{\rm FPMB}$	—	1.18 ± 0.07	”	”
χ^2/dof	—	472/339	473/339	458/338

[a] The errors on the parameters are 90% confidence.
[b] The full model in XSPEC is `constant*tbabs*pcfabs*(gaussian+reflect*bremss)`.
[c] This is the same model as the first column except for an additional Gaussian. Ditto marks indicate parameters that are consistent with the first column.
[d] This is the same model as the first column except for two additional Gaussians. Ditto marks indicate parameters that are consistent with the other two columns.
[e] The column density is calculated assuming Wilms et al. (2000) abundances and Verner et al. (1996) cross sections. Along this line of sight, the Galactic value is $N_{\rm H} = 1.8 \times 10^{22}$ cm^{-2} (Kalberla et al. 2005).
[f] The normalization for the `bremss` model is equal to $\frac{3.02\times10^{-15}}{4\pi d^2} \int n_e n_i dV$, where d is the distance to the source in units of cm, n_e and n_i are the electron and ion densities in the plasma, and V is the volume of the region containing the plasma.
[g] Fixed.
[h] The abundance of elements heavier than He relative to solar.
[i] The abundance of iron relative to the abundances specified by A.
[j] Tied to $\sigma_{\rm line1}$.

Table 4. Spectral Results for IP Mass Model Fits

Parameter[a]	Units	Value[b]
$N_{\rm H}$[c]	10^{22} cm^{-2}	$0.63^{+0.09}_{-0.08}$
$N_{\rm H,pc}$	10^{22} cm^{-2}	12^{+3}_{-2}
pc fraction	—	0.72 ± 0.03
$M_{\rm WD}$	$M_{\odot}$	>1.38
$N_{\rm IPM}$	—	$(1.63^{+0.23}_{-0.68}) \times 10^{-13}$
$\Omega/2\pi$	—	1.0[d]
A[e]	—	$0.4^{+0.5}_{-0.2}$
$A_{\rm Fe}$[f]	—	1.0[d]
cos i	—	>0.84
$E_{\rm line1}$	keV	6.4[d]
$\sigma_{\rm line1}$	keV	$0.07^{+0.04}_{-0.03}$
$N_{\rm line1}$	ph cm^{-2} s^{-1}	$(1.1 \pm 0.2) \times 10^{-5}$
$E_{\rm line2}$	keV	6.7[d]
$\sigma_{\rm line2}$	keV	0.07[g]
$N_{\rm line2}$	ph cm^{-2} s^{-1}	$(0.67 \pm 0.16) \times 10^{-5}$
$E_{\rm line3}$	keV	6.97[d]
$\sigma_{\rm line3}$	keV	0.07[g]
$N_{\rm line3}$	ph cm^{-2} s^{-1}	$(0.51 \pm 0.15) \times 10^{-5}$
$C_{\rm pn}$	—	1.0[d]
$C_{\rm MOS1}$	—	0.96 ± 0.05
$C_{\rm MOS2}$	—	1.00 ± 0.05
$C_{\rm FPMA}$	—	1.13 ± 0.07
$C_{\rm FPMB}$	—	1.20 ± 0.07
χ^2/dof	—	480/338

[a] The errors on the parameters are 90% confidence.
[b] The full model is `constant*tbabs*pcfabs*(gaussian+gaussian+gaussian+reflect*ipm)`.
[c] The column density is calculated assuming Wilms et al. (2000) abundances and Verner et al. (1996) cross sections. Along this line of sight, the Galactic value is $N_{\rm H} = 1.8 \times 10^{22}$ cm^{-2} (Kalberla et al. 2005).
[d] Fixed.
[e] The abundance of elements heavier than He relative to solar.
[f] The abundance of iron relative to the abundances specified by A.
[g] Tied to $\sigma_{\rm line1}$.